

Mechanical properties of a Ti6Al4V porous structure produced by selective laser melting

Jianfeng Sun, Yongqiang Yang*, Di Wang

School of Mechanical and Automobile Engineering, South China University of Technology, Guangzhou 510640, China

ARTICLE INFO

Article history:

Received 5 June 2012

Accepted 18 January 2013

Available online 13 February 2013

Keywords:

Flexible manufacturing

Selective laser melting

Titanium alloy

Mechanical property

Porous structure

ABSTRACT

This paper designs one octahedral Ti6Al4V porous structure and then establishes a simplified model. The Ti6Al4V porous structure is manufactured by selective laser melting. Its experimental and theoretical fracture loads are obtained through theoretical calculation and compression test respectively. The result demonstrates that there is an exponential relationship between the experimental fracture load and the porosity of the porous structure. With an average relative error of 5.86%, the deviation between experimental and theoretical fracture load is small, which indicates that the predication accuracy is comparatively high. So the fracture load calculation theory is valuable in practical applications. Finally, the fracture analysis indicates that fractures of units and porous structures are brittle fractures, which belong to cleavage fracture.

© 2013 Elsevier Ltd. All rights reserved.

1. Introduction

A porous material is a type of material that integrates structure and function. Compared with traditional materials, porous materials boast the advantages of low density, high specific strength, specific surface, light weight, sound insulation, heat insulation, and good permeability [1]. These materials are, therefore, widely applied in aerospace engineering, mechanical engineering, and optoelectronics. There are many factors affecting the properties of porous materials, among which structural design plays an essential role. Along with the development of science and technology, the size of porous materials has been decreasing while their porosity has been increasing, thus contributing to the wider use of porous materials [2].

The Ti6Al4V alloy is a two-phase type of titanium alloy that has corrosion resistance and high specific strength. Consequently, Ti6Al4V has come to be known as “space metal” [3] or “ocean metal” [4] and has been broadly used in national defense and in civil industries.

Selective laser melting (SLM) is a parts-manufacturing technique that has been growing since the 1990s. SLM can transform metal parts into arbitrary shapes without traditional cutting by melting metal powder with a laser to achieve metallurgical bonding of the powder [5]. This technique can also increase the density of the parts to more than 95%. With high density [6], good mechanical properties [7], high dimensional accuracy (dimensional error

less than 0.1 mm), and direct use with or without simple post-processing, parts manufactured by SLM outperform those manufactured by traditional techniques in terms of design and manufacturing time [8]. That is why SLM has been widely used in industries including aerospace, medicine, automobile, mold making and so on [9].

Yadroitsev et al. [10], manufactured porous materials with a pore size of 150 μm and a wall thickness of 120 μm by using a fiber laser. Lewis Mullen et al. [11], studied the effects and characteristics of the unit pore have on the growth of porous osteocytes. TIXOS [12], a company in Italy, developed a composite structure with solid and porous structures. Companies in Germany, like EOS and MCP, did in-depth research on the theoretical and practical aspects of porous materials.

However, the aforementioned researches focused on the porosity and determination of the pore size of metal parts, paying less attention to their load after processing. In this research, the maximum load of simplified model of porous structure (produced by SLM) was obtained via calculation under the strength theory. A comparison between the experimental and theoretical fracture load revealed that the predictive accuracy of the simplified model is relatively high. And reasons for the deviation between the theoretical and actual values were analyzed.

2. Experiment details

2.1. Experimental equipment

DiMetal-280 SLM rapid prototyping equipment from the South China University of Technology was utilized in this research. The

* Corresponding author. Tel./fax: +86 020 87114484.

E-mail addresses: sunjianfeng0204@163.com (J. Sun), meyqyang@scut.edu.cn (Y. Yang).

Nomenclature

d_0	theoretical sectional dimension	a	length of AB
S	cross-sectional area	b	length of BC
S_z^*	static moment of cross-section to neutral axis	V_{DEFH}	volume of right-angle tetrahedron DEFH
y_1	absolute value of distance from a point on interface to neutral axis	$V_{LMNP-FRST}$	volume of cuboid LMNP-FRST
M	moment	V_{unit}	volume of octahedral unit
$[\sigma]$	permissible stress	V_{UVYZ}	volume of octahedral UVYZ
h	section width	V_T	the volume of T
I_z	moment of inertia of entire cross-section to neutral axis	$V_{total T}$	sum of volumes of T
y	absolute value of distance from a random point outside of cross section to neutral axis	N	units number
θ_1	angle between AB and AC	η	porosity
θ_2	angle between BC and AC	c	constant
		d_1	experimental sectional dimension

main structure of DiMetal-280 is shown in Fig. 1, and its technical specifications are shown in Table 1. A Model GP-TS2000M/100kN high-temperature electronic universal tester (Changchun Intelligent Instrument Co., Ltd., Changchun, China) was employed in the compression test, and its technical specifications are also shown in Table 1.

2.2. Materials and methods

2.2.1. Materials

The Ti6Al4V gas-atomized spherical powder was used in this study. Please see Table 2 (wt.%) for its chemical composition.

2.2.2. Preparation methods

A 100 mm × 100 mm × 20 mm volume of Ti6Al4V substrate was utilized in this study. Argon served as the protective gas to ensure oxygen content remained under 0.2%. The optimized parameters are listed in Table 3. The density of samples could reach 95.03%.

2.2.3. Detection methods

The cross-sections of samples were polished by 200 lb, 400 lb, and 800 lb abrasive papers successively. The samples were ultrasonically cleaned in an acetone solution for 20 min. Then they were etched with HNO₃ + HF solution for subsequent microstructure analysis. In the compression test, we used a test speed of 1 mm/min (ASTM:E9-09) to obtain the fracture load of these samples.

3. Results and discussion

The statically indeterminate spatial structure was not taken into account in either the theoretical or experimental calculations.

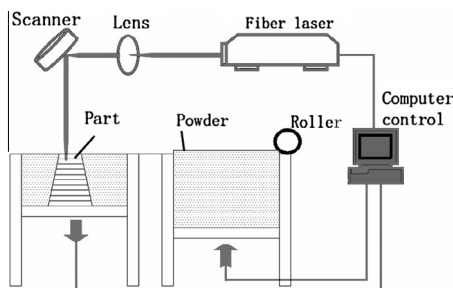


Fig. 1. Schematic diagram of SLM.

3.1. Calculation of theoretical maximum load

In order to easy to understand, nomenclatures are listed for all abbreviations before the introduction

3.1.1. Theoretical load of strut

Fig. 2 shows the designed three-dimensional structure. Fig. 2a is the assembly drawing, while Fig. 2b shows the spatial structure of the porous unit clearly. Meanwhile, the angle, the diameter of the cross-section and the length of the strut are all listed in Table 4. The dimensions of these four porous structures follow the standard ASTM:E9-09. Fig. 3 is a schematic diagram of force (AC is an imaginary line). Given that force F loads on point A, let all struts be uniformly forced, and then take strut AB for calculation. After resolving force F into F_{AB} along strut AB and F'_{AB} vertical to strut AB, the following is clear from Fig. 3:

$$F_{AB} = F \cos(\theta_1), \quad F'_{AB} = F \sin(\theta_1). \quad (1)$$

When the compressive stress and bending stress meet:

$$[\sigma] \geq \frac{F \cos(\theta_1)}{S}, \quad [\tau] \geq \frac{F \sin(\theta_1) S_z^*}{I_z b}. \quad (2)$$

From Eqs. (1) and (2), the maximum load on point B is:

$$\begin{aligned} [\sigma(\theta)]_{AB} &\geq \frac{F \cos(\theta_1)}{S} + \frac{Fa \sin(\theta_1) S_z^*}{I_z h} \\ &= \frac{F \cos(\theta_1)}{S} + \frac{Fa \sin(\theta_1) \int_A y_1 dy}{h \int_A y^2 dy}, \end{aligned} \quad (3)$$

Fig. 3b shows the forces on strut BC, where $M = Fa \sin(\theta_1)$. The bending moment generated by F_{BC} is in the opposite direction of M . Thus the maximum load at point C is

$$[\sigma(\theta)]_{BC} \geq \frac{F \cos(\theta_2)}{S} + \frac{Fb \sin(\theta_2) \int_A y_1 dy}{h \int_A y^2 dy} - \frac{Fa \sin(\theta_1) \int_A y_1 dy}{h \int_A y^2 dy}. \quad (4)$$

Let the cross-section of the strut be circular, the stress on it uniform, and its composition homogeneous so as to simplify the calculation. Then, the neutral axis and the moment of inertia overlap in this scenario. The maximum stress is generated at point C of the cross section on the horizontal line that goes through the center. Thus:

$$\frac{\int_A y_1 dy}{h \int_A y^2 dy} = \frac{1}{\frac{\pi d_0^3}{32}}. \quad (5)$$

Then Eq. (4) transforms to

Table 1

Technical specifications.

Laser wavelength (nm)	Power (W)	Maximum dimension (mm ³)	Scanning speed (mm/s)	Laser diameter (μm)	Powder thickness (μm)
DiMetal-280 1075 Capacity (optional) (kN)	200 W cw Unit	280 × 280 × 300 Load resolution	5–5000 Test speed (mm/min)	70 Test space (mm ²)	20–80 Power (W)
GP-TS2000M/100kN 100	kg, N, kN	1/100,000	0.005–1000	560 × 800	380 V AC

Table 2

Powder chemical composition of Ti–6Al–4V.

Composition (wt.%)	Al	V	O	H	N	C	Fe	Si	Ti
	5.5–6.8	3.5–4.5	0.15	0.02	0.04	0.04	0.025	0.02	Bal.

Table 3

Optimized parameters.

Power (W)	Scanning speed (mm/s)	Powder thickness (mm)	Scanning strategy	Hatch spacing (mm)
80	200	0.02	X–Y inter-layer stagger scanning	0.06

$$[\sigma_\theta]_{BC} \geq \frac{F \cos(\theta_1)}{\frac{\pi d_0^2}{4}} + \frac{Fb \sin(\theta_2)}{\frac{\pi d_0^3}{32}} - \frac{Fa \sin(\theta_1)}{\frac{\pi d_0^3}{32}}. \quad (6)$$

Let $\frac{d[\sigma]}{d\theta} = 0$ and $\frac{a}{\sin(\theta_2)} = \frac{b}{\sin(\theta_1)}$, then the first order derivative of Eq. (4) is expressed as:

$$\left\{ \sin^4(\theta_2) \times \left(\frac{b^2}{16} + \frac{d_0^4}{4096} \right) - \sin^2(\theta_2) \times \left(\frac{d_0^2 b^2 + a^2 d_0^2}{32} \right) + b^4 - 2a^2 b^2 \right\} \times F_{BC} = 0. \quad (7)$$

Substituting $F \neq 0$ into Eq. (7) and get:

$$\sin^4(\theta_2) \times \left(\frac{b^2}{16} + \frac{d_0^4}{4096} \right) - \sin^2(\theta_2) \times \left(\frac{d_0^2 b^2 + a^2 d_0^2}{32} \right) + b^4 - 2a^2 b^2 = 0. \quad (8)$$

By solving Eq. (8), it is obtained:

$$\theta_2 = \arcsin \left(\frac{8d_0}{256b^2 d_0^2 + d_0^4} \sqrt{(256b^2 + d_0^2) \times (32bd_0^2 + 32ba^2 \pm b \times) \sqrt{1023b^2 d_0^4 + 2560b^2 d_0^2 a^2 + 1024b^2 a^4 - 256b^4 d_0^2 + 2d_0^4 a^2}} \right). \quad (9)$$

Let $a = b$ and $\theta_1 = \theta_2$; Eq. (9) then simplifies to

$$\frac{d[\sigma]}{d\theta} = -\frac{d_0}{4} \sin(\theta_2) F. \quad (10)$$

When $0 < \theta_2 < \frac{\pi}{2}$ (the processing range), $\sin(\theta_2)$ is monotonically increasing; in contrast, when $(0 < \theta_2 < \frac{\pi}{2})$, Eq. (10) is monotonically decreasing. The critical point changes from point C to point B. Then, Eq. (3) transforms to

$$[\sigma_\theta]_{AB} \geq \frac{F \cos(\theta)}{\frac{\pi d_0^2}{4}} + \frac{Fa \sin(\theta)}{\frac{\pi d_0^3}{32}}. \quad (11)$$

When $\frac{d[\sigma]}{d\theta} = 0$, the maximum load on point B is

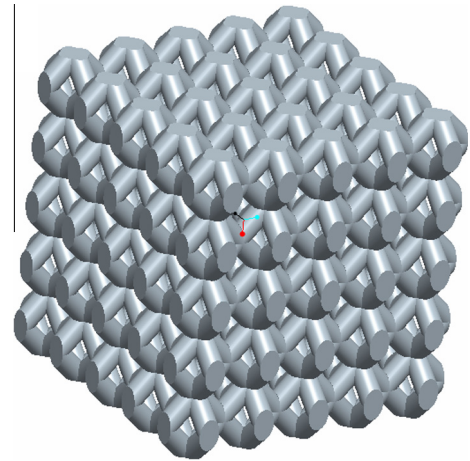


Fig. 2a. Design of octahedral: (a) assembly drawing of angle 45, $d_0 = 0.75$ mm, $a = 2$ mm.

$$\sin(\theta_1) = \frac{8a}{\sqrt{64a^2 + d_0^2}}. \quad (12)$$

Substitute Eq. (12) in Eq. (11) to obtain the relationship among the maximum loads, a and b :

$$[\sigma] = \frac{32a^2 + 4d_0^2}{\pi d_0^3 \sqrt{64a^2 + d_0^2}} F. \quad (13)$$

Let $\frac{d[\sigma]}{da} = 0$ and d a constant, then it is obtained via Eq. (9):

$$a = \sqrt{\frac{3}{32}} d_0. \quad (14)$$

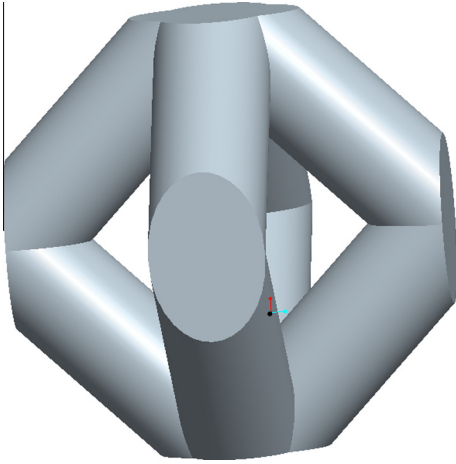


Fig. 2b. Design of octahedral: (b) unit of angle 45, $d_0 = 0.75$ mm, $a = 2$ mm.

Table 4
Design of octahedral date.

Number	Angle (°)	Cross section diameter of strut (mm)	Length of strut (mm)
1	45	0.75	2
2	45	1	2
3	30	0.75	2
4	30	1	2

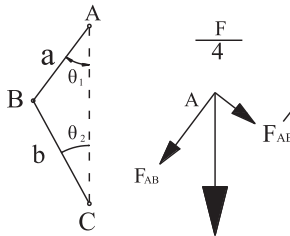


Fig. 3a. Schematic diagram of force: (a) force of AB.

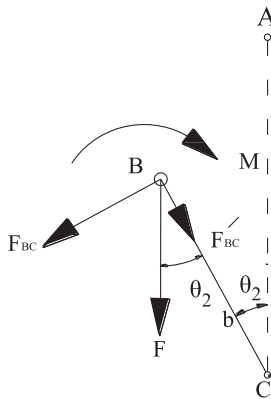


Fig. 3b. Schematic diagram of force: (b) force of BC.

$$\begin{cases} \theta_1 = 6^\circ \\ a = \sqrt{\frac{d_0}{32}} \\ F = \frac{[\sigma]\pi d_0^2}{\sqrt{7}} \end{cases}$$

3.1.2. Units porosity

3.1.2.1. *Cuboid volume.* Calculate the volume of the cuboid containing the octahedron first to set the basis for calculating the global porosity. It can be seen from Fig. 4 that

$$DE = DF = DG = DH = a, \angle FDO = \angle EDO = \angle HDO = \theta_1$$

$$DO = a \cos \theta_1, FO = HO = a \sin \theta_1 \text{ from the known conditions.}$$

$$\text{Therefore, } V_{\text{LMNP-FRST}} = 8a^3 \sin^2 \theta_1 \cos \theta_1. \quad (15)$$

3.1.2.2. *Octahedron volume.* The volume of the octahedron is shown in Fig. 4. The octahedron designed for this paper can be presented as the sum of the volumes of four right-angle tetrahedrons DEFH. It is known from Fig. 4 that:

$$V_{\text{DEFH}} = \frac{1}{3} a^3 \sin^2 \theta_1 \cos \theta_1. \quad (16)$$

From formula (16), we obtain

$$V_{\text{unit}} = 4V_{\text{DEFH}} = \frac{4}{3} a^3 \sin^2 \theta_1 \cos \theta_1 \quad (17)$$

3.1.2.3. *Internal hollow volume.* See Fig. 5 for the joints of the struts.

$$\text{Given } \angle VUO = \angle BVW = \angle YCX = \theta_1, BC = a, VW = XY = d_0,$$

$$\text{then } WX = a - \frac{d_0}{2} \tan \theta_1 - \frac{d_0}{2 \tan \theta_1}. \quad (18)$$

From formula (18), we obtain the following:

$$V_{\text{UVYZ}} = \frac{4}{3} \left(a - \frac{d_0}{2} \tan \theta_1 - \frac{d_0}{2 \tan \theta_1} \right)^3 \sin^2 \theta_1 \cos \theta_1. \quad (19)$$

The volume of the cuboid (see Fig. 4) containing the octahedron is calculated first to set the basis for calculation of global porosity. The volume of T (see Fig. 6) is repeatedly calculated and subtracted while calculating porosity.

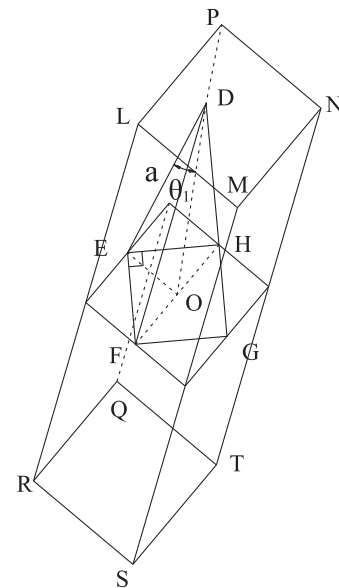


Fig. 4. Schematic diagram of the calculation of the porosity.

Substituting Eqs. (12) and (14) in Eq. (11), and given that the load reaches maximum, then the relationship becomes as:

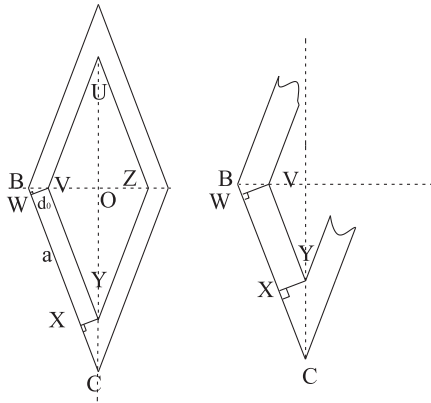


Fig. 5. Schematic diagram of the struts' joints.

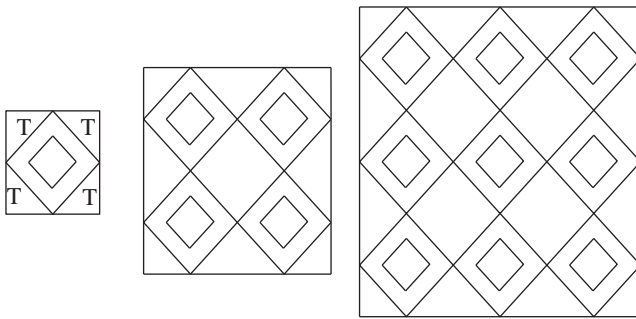


Fig. 6. Schematic diagram of the volume increase.

The volume of T is obtained from the geometric relationship in Fig. 6:

$$V_T = \frac{1}{4} \times \left(8a^3 \sin^2 \theta_1 \times \cos \theta_1 - \frac{4}{3} a^3 \sin^2 \theta_1 \cos \theta_1 \right). \quad (20)$$

When $N = 1, 2$ volumes of T have been repeatedly calculated; $N = 8, 12$ volumes; $N = 27, 30$ volumes of T ; and when $N = 64, 72$ volumes of T have been calculated repeatedly. By such reasoning, we obtain the relationship between total volume T and N as follows:

$$V_{total T} = 4 \times (2^{\sqrt[3]{N}} - 1) \times \sqrt[3]{N} \times V_T. \quad (21)$$

The porosity is derived from formulas (15), (18), (19), (20), and (21):

$$\eta = \frac{NV_{LMNP-FRST} - NV_{unit} + NV_{UVYZ} - V_{total T}}{NV_{LMNP-FRST} - V_{total T}} = \frac{5(\sqrt[3]{N} - 1)^2 a^3 - \sqrt[3]{N^2} \left(a - \frac{d_0}{\sin 2\theta_1} \right)^3}{(6\sqrt[3]{N^2} - 10\sqrt[3]{N} + 5)a^3}. \quad (22)$$

It is known from the Ryskewich model that the stress on the porous material satisfies the following:

$$[\sigma]_{porosity} = e^{-c\eta} [\sigma]_{density}. \quad (23)$$

From [13], we obtain $c = 0.7$. Formula (11) calculates the load of the dense body's struts. The structure manufactured in this paper was a porous material composed of struts; thus, $[\sigma]_{porosity}$ should be chosen for calculating the global maximum load.

Substituting the porosities of manufactured samples 1, 2, 3, and 4 into formulas (11) and (23), we obtain the following:

$$F_{theoretical} = \frac{N\pi k[\sigma]_{density} d_0^3}{d_0 \cos \theta + 8a \sin \theta} = \frac{N\pi e^{-c\eta} [\sigma]_{density} d_0^3}{d_0 \cos \theta + 8a \sin \theta} = \frac{5(\sqrt[3]{N} - 1)^2 a^3 - \sqrt[3]{N^2} \left(a - \frac{d_0}{\sin 2\theta_1} \right)^3}{(6\sqrt[3]{N^2} - 10\sqrt[3]{N} + 5)a^3} \times \frac{N[\sigma]_{density} d_0^3 \pi e^{-0.7\eta}}{d_0 \cos \theta + 8a \sin \theta}, \quad (24)$$

where $[\sigma]_{density} = 895 \text{ MPa}$ [14]. Assume that the pore in the solid parts of the sample only has influence on the sectional dimension on the condition that the density of the entity parts of the sample is only 95%. Then:

$$\frac{\pi d_0^2}{4} = \frac{0.95\pi d_1^2}{4}. \quad (25)$$

Through formula (25), we obtain $d_1 = 0.97d_0$.

3.2. Experimental load

The four structures, differing in strut angle and section diameter, were processed on the same substrate, and their processing parameters are listed in Table 4. Fig. 7 shows the morphology of the four structures after processing. With strut angles of 45° , samples 1 and 2 are cubes; however, with strut angles of 60° , samples 3 and 4 are cuboids. We conducted a compression test on samples 1, 2, 3, and 4, and then we compared the experimental load and the theoretical load on these samples to analyze the deviations among them.

Fig. 8 shows the stress–strain curves of samples 1, 2, 3, and 4 as well as the maximum load of the experiment in Table 5. We substituted the data from Table 4 into formula (26) to obtain the theoretical load (see Table 5).

Table 5 clearly demonstrates that the errors between the theoretical values and experimental values are tiny. In conclusion, the calculation accuracy of the simplified model is relatively high.

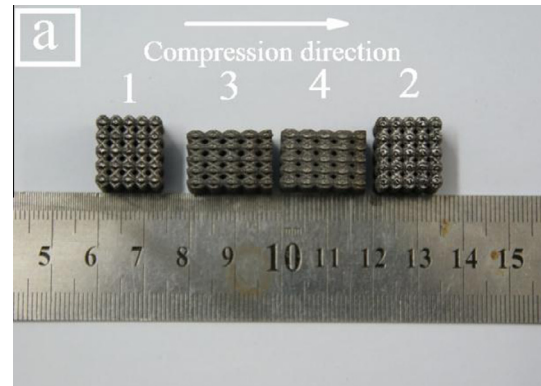


Fig. 7a. Morphology of octahedral by SLM (a) front view

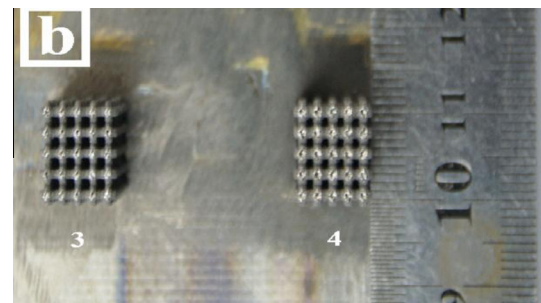


Fig. 7b. Morphology of octahedral by SLM (b) side view.

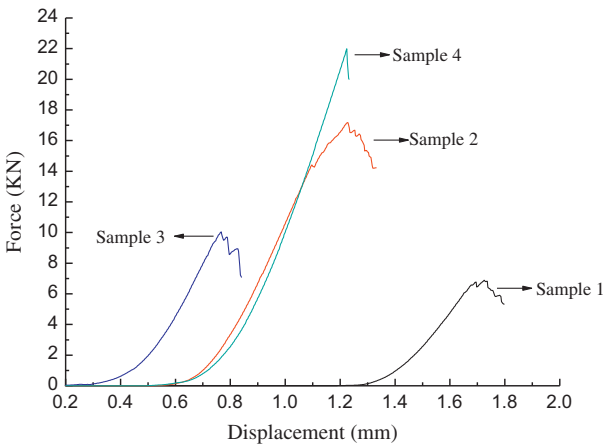


Fig. 8. Stress–strain curve of sample 1, sample 2, sample 3 and sample 4.

3.3. Microstructure analysis

As is generally known, microstructure determines property of the material. The microstructure of the grain boundary is shown in Fig. 9. The XRD pattern in Fig. 10 shows that the three phases, α' , β and Ti_3Al , were produced. Sun [15] and Poondla [16] heated the samples to the transformation temperature and cooled them with different rate, and finally observed their microstructures. The microstructures obtained under high cooling rate are same as the microstructure in this paper. The grain size in this paper is smaller than their grain size, since the cooling rate of SLM is faster than theirs. The solid solution atoms V in phase β of $\text{Ti}_6\text{Al}_4\text{V}$ did not have enough time to diffuse out of unit cells and thus transform into phase α . However, the martensite transformation is a type of diffusionless transformation. There were no atoms randomly passing or sequentially leaping through the interface and thus the new phase (martensite) shall inherit the chemical composition, atomic order and crystal defects of its parent phase [17]. With a transformation speed close to the sound velocity [18], the BCC phase β in $\text{Ti}_6\text{Al}_4\text{V}$ directly turned into HCP phase α' .

3.4. Microhardness test

The microhardness at a measured depth of the sample was tested by the microhardness tester. The microhardness of at least three points at the same depth were measured and averaged. The microhardness conformed to the Vicker hardness. As shown in Fig. 11, the average microhardness of the formed sample is 482.9068 $\text{Hv}_{0.2}$, which is higher than the microhardness of 440 $\text{Hv}_{0.3}$ researched by Amaya-Vazquez et al. [19]. There are two reasons for this situation. The first reason for this is the composition: there were many alloying elements in the $\text{Ti}_6\text{Al}_4\text{V}$ powder, including Al, V, O, H, N, and C. After being heated with a laser, these elements diffused rapidly in the molten pool and generated tiny alloy compounds represented as Ti_3Al . These compounds formed hard spots dispersed in the microstructure that greatly improved the microhardness of the formed sample. [19] shows that the XRD peak intensity of Ti_3Al is less than in this paper, so there are less

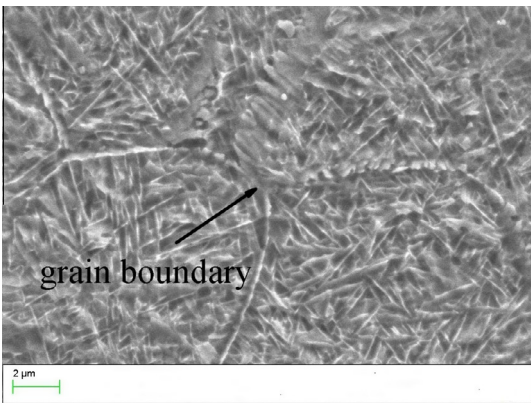


Fig. 9. Morphology of grain boundary.

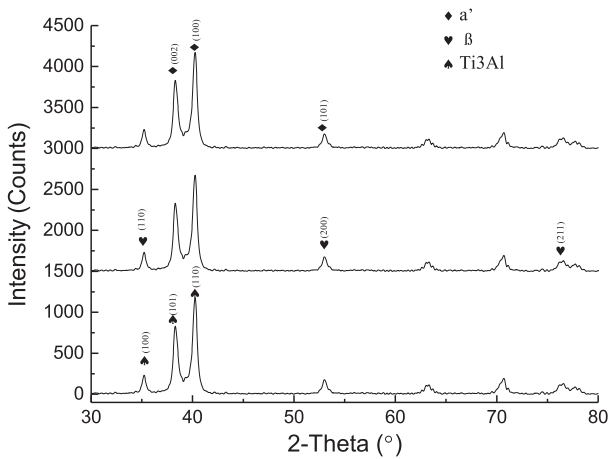


Fig. 10. X-ray diffraction pattern of sample.

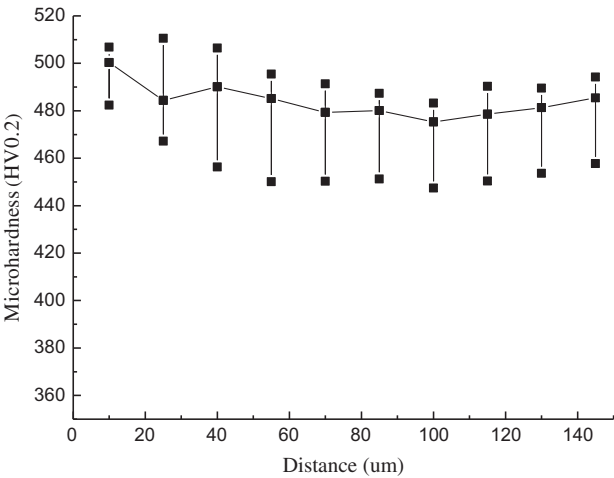


Fig. 11. Microhardness of sample.

Table 5
Experimental load of samples 1–4.

Number	Theoretical diameter (mm)	Experimental diameter (mm)	Experimental load (N)	Theoretical load (N)	Relatively error (%)	Average relatively error
1	0.75	0.73	6886.7	6496.6	5.66	5.85%
2	1	0.97	16429.7	15183.8	7.58	
3	0.75	0.73	9708.2	9161.3	5.62	
4	1	0.97	21990.7	20988.1	4.56	

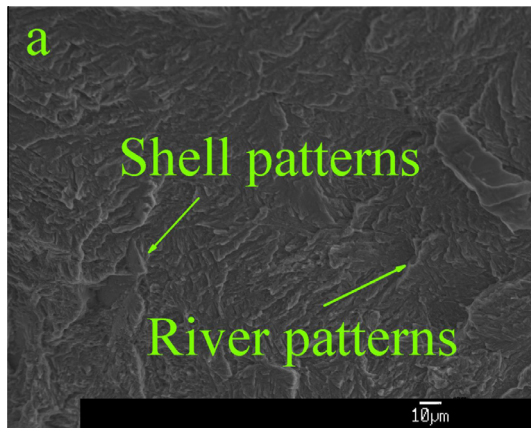


Fig. 12a. Morphology of fracture: (a) river and shell patterns.

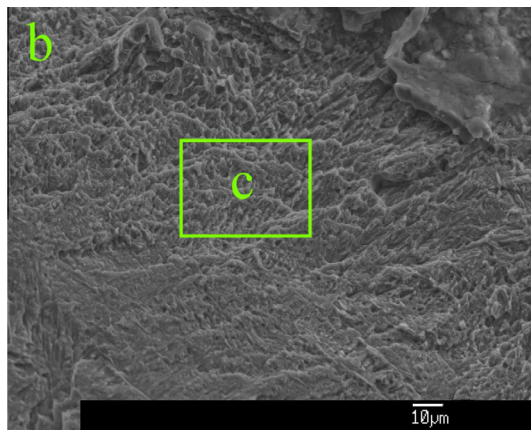


Fig. 12b. Morphology of fracture: (b) overall morphology of dimple.

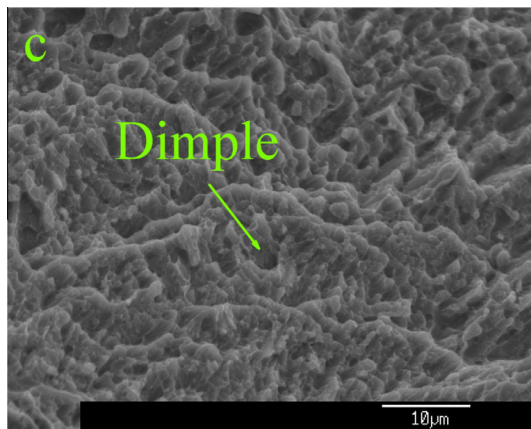


Fig. 12c. Morphology of fracture: (c) dimple.

Ti₃Al in it. The second reason is the microstructure: the martensites in Ti₆Al₄V belonged to hard phase, which also improved the overall microhardness. In [19] the microstructure contains less martensites and many large grains, so its hardness is lower.

3.5. Fracture morphology analysis

The morphology of the fracture, shown in Fig. 12, is smooth and uniform. The river and shell patterns appear in Fig. 12a are charac-

teristics of cleavage fracture. Macroscopically, like in the laser welding, Ti₆Al₄V experienced brittle fracturing [20], but microscopic dimples and tearing ridges could also be found, which is same as the fracture morphology in [21]. The dimples in Figs. 12b and c, with their irregular shape and relatively small number, are distributed inhomogeneously. Therefore, the fracture mode of the Ti₆Al₄V alloy is a mixed one based on brittle fracturing. [20,21] paid attention to obtain the process parameters for maximum tensile strength, but there is less analysis of the fracture mechanism.

The generation of fracture is caused by microstructural transformation. The extremely rapid cooling caused Ti₆Al₄V to generate a large amount of supersaturated solid solution of Al. When the concentration of Al increased to a level higher than the concentration of the supersaturated solid solution, the aluminide Ti₃Al (as shown in Fig. 10) would precipitate in the grain boundary. Ti₃Al is a typical brittle microstructure that is inclined to generate and propagate cracks rapidly, which in turn explains the obvious traces of brittle fractures in the fracture morphology. Analysis of the fracture morphology implies that the fracturing process occurred when the material generated cracks and a large number of dislocations gathered on the grain boundaries under external stress. The continuous increase in external stress caused the dislocations to proliferate extensively. Grain boundary energy thus increased while stability was poor, thus leading to gradual concentration of stress. As the experiment progressed, cracks extended along the martensite phase grain section until the last failure.

4. Conclusions

The theoretical load of the octahedral Ti₆Al₄V porous structure was obtained by calculating the load of the simplified model of this structure. The results in this study demonstrate that the experimental fracture load of the Ti₆Al₄V porous structure, which is obtained through a compression test, agrees well with the theoretical maximum load.

Following conclusions can be derived:

- (1) The theoretical maximum load of the porous structure is $F_{theoretical} = \frac{N\pi e^2 H_1(\sigma) \text{density} d_0^3}{d_0 \cos \theta + 8a \sin \theta}$, where N is the number of porous structure units.
- (2) Microstructure analysis implies that the microstructure of the porous structure contains a large amount of martensites that intermesh with each other and raise the energy required for crack propagation. Therefore, the experimental fracture load is larger than the theoretical maximum load.
- (3) Fracture morphology analysis indicates that the porous structure experiences brittle fracturing – a type of cleavage fracture. The microhardness measurement indicates that the average microhardness of the porous structure is 482.9068 Hv_{0.2}.

Acknowledgements

This work was supported by the National Natural Science Foundation of China under Grant no. 51275179.

References

- [1] Barbas A, Bonnet AS, Lipinski P. Development and mechanical characterization of porous titanium bone substitutes. *J Mech Behav Biomed Mater* 2012; 9:34–44.
- [2] Pattanayak DK, Fukuda A, Matsushita T, Takemoto M, Fujibayashi S, Sasaki K, et al. Bioactive Ti metal analogous to human cancellous bone: fabrication by selective laser melting and chemical treatments. *Acta Biomater* 2011;7(3): 1398–406.

- [3] Marcua T, Todeab M, Gligora I, Bercec P, Popa C. Effect of surface conditioning on the flowability of Ti6Al7Nb powder for selective laser melting applications. *Appl Surf Sci* 2012;258(7):3276–82.
- [4] Song B, Dong S, Zhang B, Liao H, Coddet C. Effects of processing parameters on microstructure and mechanical property of selective laser melted Ti6Al4V. *Mater Des* 2012;35:120–5.
- [5] Nga CC, Savalanian MM, Laub ML, et al. Microstructure and mechanical properties of selective laser melted magnesium. *Appl Surf Sci* 2011;257:7447–54.
- [6] Brandl E, Heckenberger U, Holzinger V, Buchbinder D. Additive manufactured AlSi10Mg samples using selective laser melting (SLM): microstructure, high cycle fatigue, and fracture behavior. *Mater Des* 2012;34:159–69.
- [7] Amato KN, Gaytan SM, Murr LE. Microstructures and mechanical behavior of Inconel 718 fabricated by selective laser melting. *Acta Mater* 2012;60(5):2229–39.
- [8] Vilaro T, Colimb C, Bartout JD. Microstructural and mechanical approaches of the selective laser melting process applied to a nickel-base superalloy. *Mater Sci Eng: A* 2012;534:446–51.
- [9] Zhang B, Liao H, Coddet C. Effects of processing parameters on properties of selective laser melting Mg–9%Al powder mixture. *Mater Des* 2012;34:753–8.
- [10] Yadroitsev I, Shishkovsky I, Bertrand P, Smurov I. Manufacturing of fine-structured 3D porous filter elements by selective laser melting. *Appl Surf Sci* 2009;255:5523–7.
- [11] Mullen L, Stamp RC, Brooks WK, Jones E, Sutcliffe CJ. Selective laser melting: a regular unit cell approach for the manufacture of porous, titanium, bone in-growth constructs, suitable for orthopedic applications. *J Biomed Mater Res Part B: Appl Biomater* 2008;5:325–34.
- [12] Mangano C, Perrotti V, Iezzi G, Scarano A, Mangano F, Piattelli A. Bone response to a new modified titanium surface implants. *J Oral Implantol* 2008;34:17–24.
- [13] Panxin Wang. Powder metallurgy science. 3rd ed. Beijing: Metallurgical Industry Press; 2010. p. 148–57.
- [14] Leyens C, Peters M. Titanium and titanium alloys. 1st ed. Beijing: Chemical Industry Press; 2005. p. 19–39, 140–5, 155–7.
- [15] Sun SD, Zong YY, Shan DB, Guo B. Hot deformation behavior and microstructure evolution of TC4 titanium alloy. *Trans Nonferr Met Soc China* 2010;20(11):2181–4.
- [16] Poondla N, Srivatsan TS, Patnaik A, Petraroli M. A study of the microstructure and hardness of two titanium alloys: commercially pure and Ti–6Al–4V. *J Alloys Compd* 2009;486(1–2):162–7.
- [17] Christian JW. Theory of transformations in metals and alloys. 2nd ed. Oxford: Pergamon; 2002.
- [18] Nishiyama Z, Fine ME, Meshii M, Wayman CM. Martensitic transformation. 1st ed. New York: Academic Press; 1978.
- [19] Amaya-Vazquez MR, Sánchez-Amaya JM, Boukha Z, Botana FJ. Microstructure, microhardness and corrosion resistance of remelted TiG2 and Ti6Al4V by a high power diode laser. *Corros Sci* 2012;56:36–48.
- [20] Zhao SS, Yu G, He XL, Hu YW. Microstructural and mechanical characteristics of laser welding of Ti6Al4V and lead metal. *J Mater Process Technol* 2012;212(7):1520–7.
- [21] Akman E, Demir A, Canel T, Sinmazçelik T. Laser welding of Ti6Al4V titanium alloys original research article. *J Mater Process Technol* 2009;209(8):3705–13.